Journal of Alloys and Compounds 1036 (2025) 182020

Contents lists available at ScienceDirect

Journal of Alloys and Compounds

journal homepage: www.elsevier.com/locate/jalcom

Design of near-β Ti-Zr-Mo-Cu multi-principal element alloys with low elastic modulus and enhanced corrosion resistance

Yusha Luo, Minqi Xu, Qihan Zheng, Qianqian Wang, Zhijun Guo *, Baolong Shen

School of Materials Science and Engineering, Jiangsu Key Laboratory for Advanced Metallic Materials, Southeast University, Nanjing 211189, China

ARTICLE INFO

Keywords:
Multi-principal element alloys
Elastic modulus
Mechanical property
Corrosion resistance
Load-bearing implant materials

ABSTRACT

Simultaneously achieving ultra-low elastic modulus, high corrosion resistance, and large plasticity of multi-principal element alloys has been a tremendous challenge for load-bearing metallic implant materials. Here, novel near-β alloys are developed *via* alloying xMo (x = 6, 7, 8, 9, 13, 17 wt%) into Ti-18Zr-10Cu prototype. The β-stabilizing 8Mo alloy, characterized by a low-modulus β-phase matrix and finely dispersed α''-phase precipitates, achieves an elastic modulus of 60 GPa, compressive strength of ~1400 MPa, and plastic strain of 35 %. This dual-phase microstructure synergistically balances strength and plasticity through β-phase strain accommodation and α''-phase dislocation pinning, thereby circumventing the strength-ductility trade-off endemic to conventional β-Ti alloys. In addition, the 8Mo alloy displays good corrosion resistance, as revealed by low corrosion passive current density of 10^{-3-3} A/cm^2 and high corrosion potential of ~ 0 V, which are attributed to the formation of passive film consisting of MoO_4. This study provides an encouraging candidate for load-bearing implant materials due to their high corrosion resistance, large plasticity, and low elastic modulus which can help inhibit stress shielding.

1. Introduction

Metals and their alloys are widely used in biomedical materials, particularly for the replacement of hard tissues, which require excellent mechanical properties, low elastic modulus, and high corrosion resistance [1]. Approximately 75 % of total hip replacement implants are manufactured out of Titanium (Ti) and Ti alloys [2], such as Ti-6Al-4V, commercially pure Ti, and titanium-nickel shape-memory alloys due to their metallic mechanical strength and high corrosion resistance [3,4]. However, there are two major issues with these medical implants. Firstly, the potential release of cytotoxic ions such as Ni^{4+}, and V^{5+} metal ions that trigger inflammation and pose a health risk. Secondly, a significant mismatch between the elastic modulus of these implants (typically >110 GPa) and natural bone modulus (~ 30 GPa) can induce bone resorption owing to stress shielding, which promotes bone resorption and may result in implant loosening and eventually premature failure [5–7]. For instance, pure Ti and Ti-6Al-4V have an elastic modulus of 110 GPa [8], while Ti-12Mo-6Zr-2Fe and Ti-13Nb-13Zr demonstrate moduli of approximately 82 GPa [9] and 79 GPa [10], respectively. Even more strictly, achieving simultaneous optimization of mechanical and corrosion properties in such alloys remains fundamentally unattainable. Therefore, the development of metallic implant materials with non-toxicity, high strength, good corrosion resistance, large plasticity, and low modulus is an urgently needed area of research.

Recent studies have highlighted the potential of biomedical alloys containing multiple principal non-toxic and allergy-free elements, such as Ti, Zr, Ta, Cu, and Nb, that show superior mechanical and corrosion properties [11–14]. Generally, these alloys are composed of metastable β-phase (body-centered cubic structure, BCC) that exhibits the lowest elastic moduli because of its lowest lattice densities and weaker bonds [15,16], compared to other phases having crystal structures of hexagonal close-packed (HCP: α, α' and ω), and orthorhombic (α'' and α+β) [17,18]. The prevailing opinion among researchers is that the elastic modulus of the common phases follows the order: $\beta < \alpha'' < \omega$ [19]. Therefore, the conventional design approach for low-modulus alloys typically avoids the formation of high-modulus phases as much as possible to stabilize the β-phase. The complete mutual solubility between Ti and Zirconium (Zr) across all compositional ranges enables the formation of homogeneous solid solutions, which is critical for achieving uniform mechanical properties and low modulus. Besides, Ti-Zr alloys, as transition metal systems, demonstrate exceptional biocompatibility

* Corresponding author.
E-mail address: zj-guo@seu.edu.cn (Z. Guo).

https://doi.org/10.1016/j.jallcom.2025.182020
Received 28 May 2025; Received in revised form 30 June 2025; Accepted 1 July 2025
Available online 2 July 2025

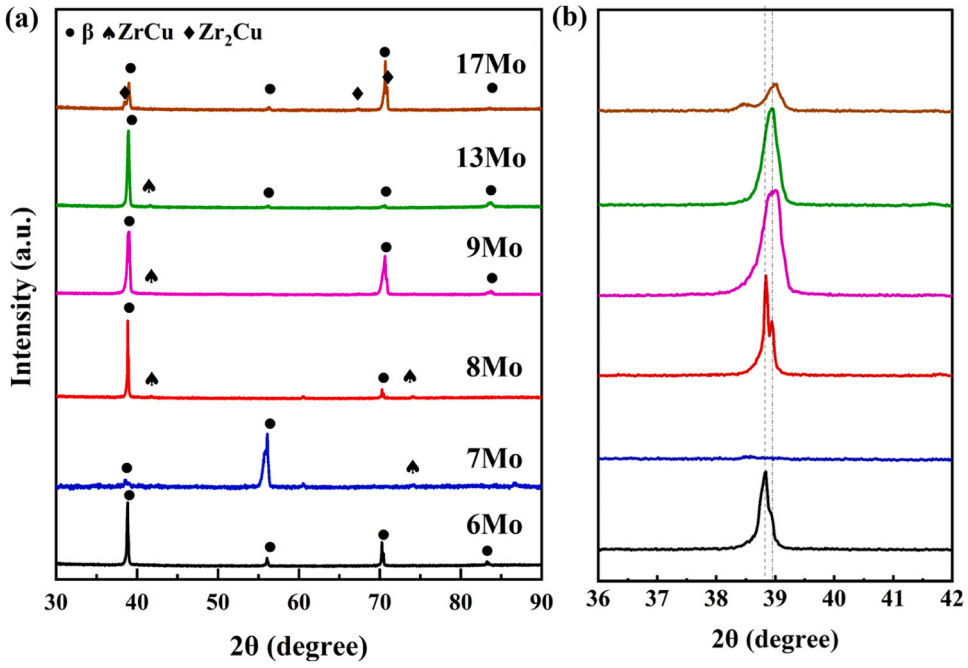

Fig. 1. (a) XRD patterns and (b) the enlarged (110) diffraction peaks of the Ti-18Zr-xMo-10Cu (x = 6, 7, 8, 9, 13 and 17 wt%) alloys.

and phase stability, making them promising candidates for orthopedic and dental implants [20]. To further augment functionality, copper (Cu)- a well-documented antibacterial agent, is frequently incorporated into these alloys, leading to the development of Ti-Zr-Cu ternary systems with combined osseointegration and antimicrobial capabilities. In addition, the addition of β-phase stabilizers, such as molybdenum (Mo) or tantalum (Ta), is easier to obtain ultra-low elastic modulus by promoting β-phase (BCC) formation. However, Ta faces practical limitations due to its ultrahigh melting point (3017 ℃, 1668 ℃ for Ti) and density (16.65 g/cm^3, approximately fourfold that of Ti (4.5 g/cm^3)), coupled with significantly higher material costs compared to Mo. In contrast, Mo not only enhances β-phase stability but also improves corrosion resistance in physiological environments and potentially regulates local pH homeostasis through molybdate ion (MoO_4^{2-}) release [19], thereby offering a cost-effective strategy for balancing biomechanical and biochemical requirements.

In this paper, we focus on pre-screened Ti-18Zr-10Cu system with a low bonding force selected as our prototype. By adding the Mo content, six Ti-18Zr-xMo-10Cu (x = 6, 7, 8, 9, 13, 17 wt%) multi-principal element alloys were designed and fabricated by arc melting. Among them, the β-phase stability is delicately balanced with α'' phase in 8Mo alloy to simultaneously achieve lower elastic modulus (~60 GPa), higher compressive strength of 1400 MPa, and large plastic strain (~35 %). Although the modulus of 8Mo alloy remains higher than that of human bone, its relatively low β-phase stability and multiphase composition provide an ideal foundation for evaluating the influence of Mo on the phase transformation behavior. Additionally, we sought to study the effects of Mo on the mechanical properties, and corrosion resistance of the Ti-18Zr-xMo-10Cu alloys, evaluating the potential of 8Mo alloy as a novel implant material. Overall, this research aims to provide further insights into the influence of Mo on the microstructure and properties of near-β implant multi-principal element alloys.

2. Materials and procedures

2.1. Sample preparation

Alloy ingots with nominal compositions of the Ti-18Zr-xMo-10Cu (wt%, x = 6, 7, 8, 9, 13, 17, denoted as xMo alloy) were fabricated by arc-melting the mixtures of the high-purity (99.99 wt%) metals in an argon atmosphere purified using a Ti-getter. The ingots of these multi-principal element alloys were flipped and remelted at least five times to ensure homogeneity of compositions. Cylindrical specimens (2 mm diameter × 4 mm height) were sectioned from the as-cast ingots using electrical discharge machining (EDM) and the surfaces of these specimens were mechanically polished with the 2000-grit SiC sandpapers. Compressive mechanical properties of the Ti-Zr-Mo-Cu alloys were conducted at a strain rate of 10^{-3} s^{-1} using an Instron-5982 machine. For microstructural and electrochemical anyalses, disc samples (10 mm diameter × 2 mm thickness) were cut from the ingots using EDM. All samples were ground with SiC paper up to 2000 grit and polished using 0.04 μm SiO_2 suspensions to achieve a mirror-like surface morphology devoid of observable scratches under optical microscopy. Lastly, the disc samples were rinsed with deionized water after ultrasonic cleaning with acetone and ethanol.

2.2. Microstructure characterization

Phase identifications were performed by X-ray diffraction (D8 Discover, Bruker, Germany) using with 1.54 Å Cu-Kα radiation and scattering angle in the range of 30° to 90°. Detailed characterizations and chemical distribution analysis were performed by scanning electron microscope (SEM), transmission electron microscopy (TEM), high-angle annular dark field-scanning transmission electron microscopy (HAADF-STEM), and energy-dispersive X-ray spectroscopy (EDS). The SEM characterization was carried out by a field emission environmental (Nova Nano 450, Thermo Fisher, USA). Before SEM observations, disc samples underwent chemical etching using Kroll's reagent (HF: HNO_3: H_2O = 2: 1: 17) for 5–30 s. The TEM, HAADF-STEM image, and EDS mapping were obtained using Talos F200X (F200X, Thermo Fisher, USA), operated at 200 kV. Samples for TEM characterization were further mechanically ground with SiC papers down to a thickness of 60 μm, punched into disks with a diameter of 3 mm, and then thinned by ion beam thinner (M691, GATAN, USA). The Vicker hardness of samples was measured using an automatic tester (FM-700, FUTURE-TECH, Japan) with a load of 300 g and a loading time of 10 s.

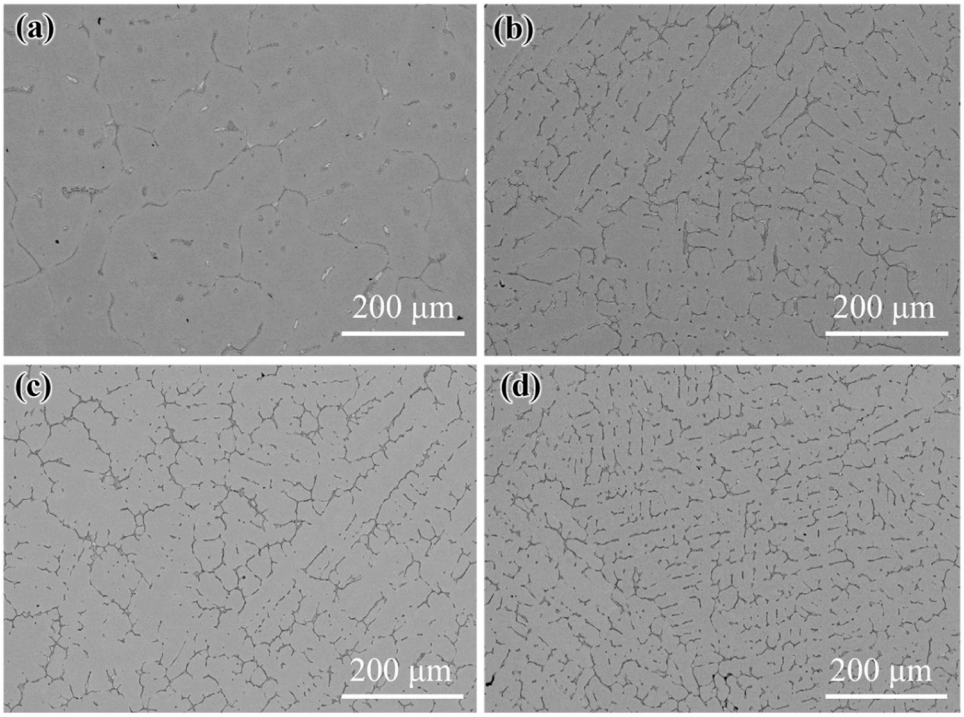

Fig. 2. SEM images of Ti-18Zr-xMo-10Cu alloys. (a) 6Mo; (b) 7Mo; (c) 8Mo; (d) 9Mo.

2.3. Electrochemical tests

Corrosion properties of the Ti-Zr-Mo-Cu alloys were investigated at 310 K in Hank's solution (prepared by dissolving 0.40 g/L KCl, 0.14 g/L $CaCl_2$, 0.20 g/L $MgSO_4{\cdot}7H_2O$, 0.35 g/L $NaHCO_3$, 0.06 g/L KH_2PO_4, 1.00 g/L $C_6H_{12}O_6$, 8.00 g/L NaCl, and 0.12 g/L $Na_2HPO_4{\cdot}12H_2O$ in the distilled water) by electrochemical measurements. The pure Ti alloy was also examined as the reference material. The electrochemical properties were examined by an Interface1000 (Gamry, USA) electrochemical workstation with a standard three-electrode cell system. In these tests, a platinum electrode served as the counter electrode, a saturated calomel electrode (SCE) functioned as the reference electrode, and the sample with a surface area of 0.785 cm acted as the working electrode. The corrosion specimen was immersed in the solution for 1 h to get a steady state of the open-circuit potential (OCP), and electrochemical impedance spectroscopy (EIS) was performed by applying a sinusoidal AC perturbation of 10 mV amplitude with a frequency sweep from 0.01 Hz to 10 kHz. Post-EIS characterization, the potentiodynamic polarization behavior was evaluated with a sweeping range of −1 V to + 1.5 V at a sweeping rate of 0.5 $mV{\cdot}s^{-1}$. To validate reproducibility, triplicate measurements were performed under identical conditions.

3. Results and discussion

3.1. Microstructure of the Ti-Zr-Mo-Cu alloys

The XRD patterns of the as-cast Ti-Zr-Mo-Cu alloys are shown in Fig. 1. It is found that the crystal structures of these alloys are sensitive to the Mo contents. Only one group of diffraction peaks corresponding to the BCC (β) phase is observed in the pattern of 6Mo alloy. When the content of Mo falls into 7–13 wt%, the alloys comprise the β phase and ZrCu intermetallic (orthorhombic α'' phase). The diffraction peaks of 17Mo are comprised of β, α'', and Zr_2Cu phases. As reported, Zr is a neutral element and its effect on the β stability of the alloys could be negligible [21]. A minimum of 10 wt% Mo is required to stabilize the β phase in binary Ti-Mo alloys at room temperature [22], which is higher than our Ti-Zr-Mo-Cu alloys. Therefore, the β-stabilizing effect of Zr coexisting with Mo is much stronger than expected. The enlarged (110)

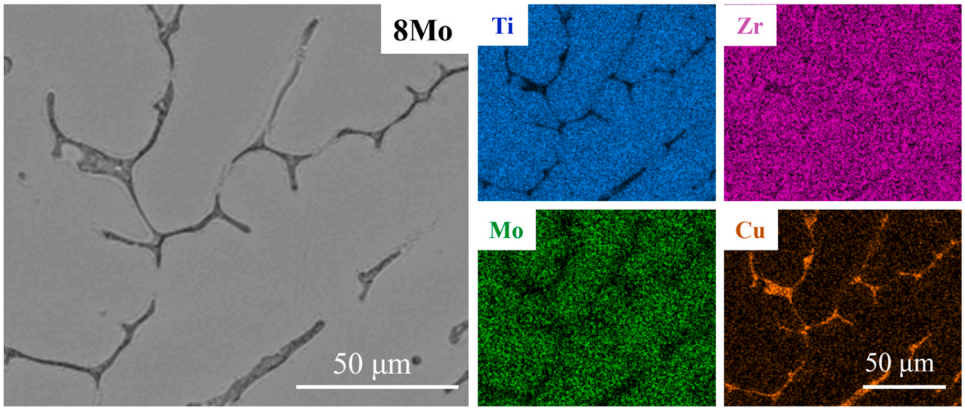

Fig. 3. SEM-EDS characterization results of 8Mo alloy. The elements distribution maps of Ti, Zr, Mo, and Cu.

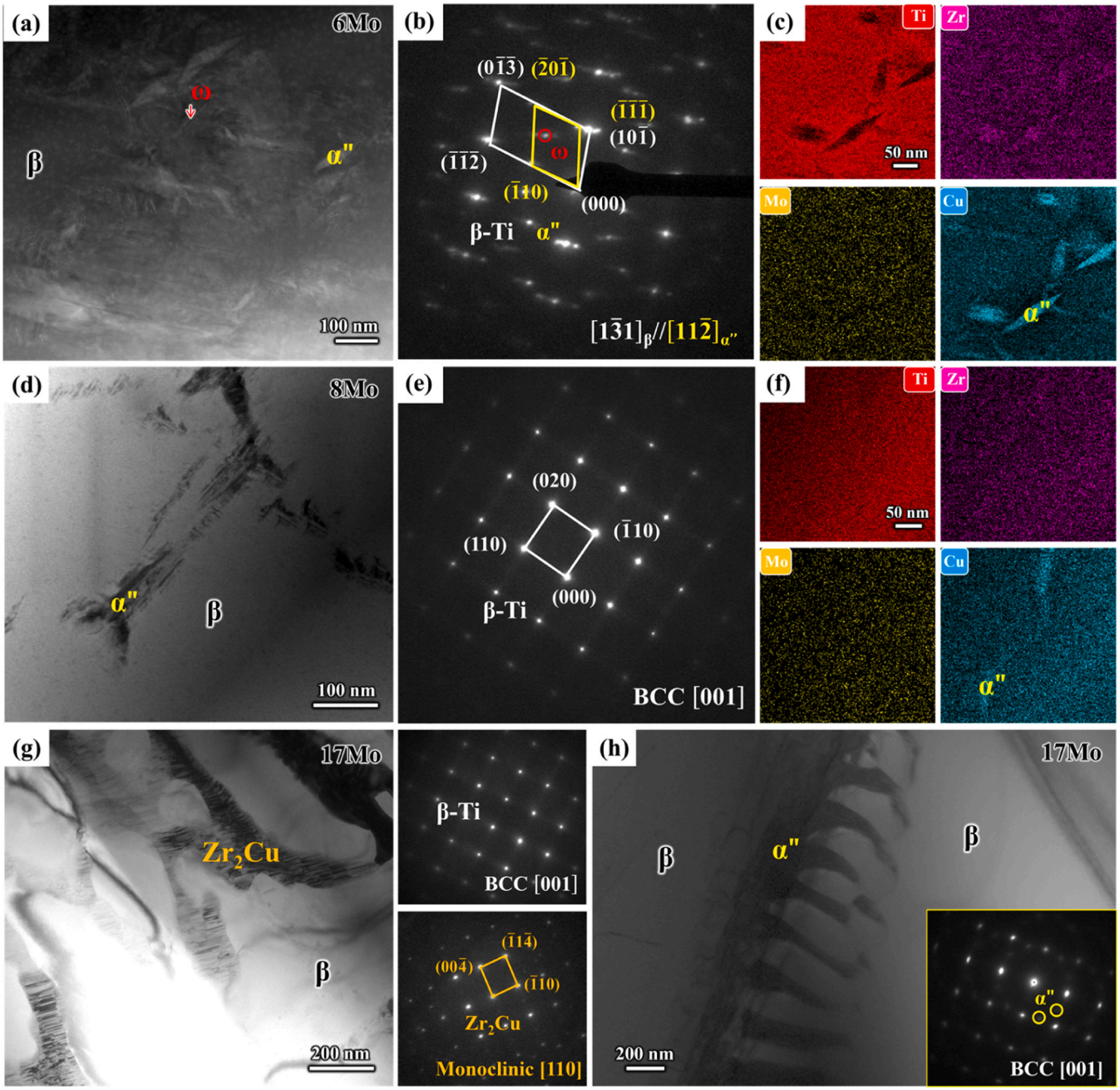

Fig. 4. TEM characterization of 6Mo, 8Mo, and 17Mo alloys. (a)-(c) bright-field (BF) image, selected area electron diffraction (SAED) pattern, and corresponding energy dispersive X-ray spectroscopy (EDS) analysis of 6Mo alloy. (d)-(f) BF image, SAED pattern, and EDS analysis of 8Mo alloy. (g)-(h) BF images and corresponding SAED patterns of 17Mo alloy.

diffraction peak of the β phase in Fig. 1(b) gradually shifts to the right as the Mo content increases. This is attributable to the fact that the atomic radius of Mo is significantly smaller than that of Zr, resulting in a smaller lattice constant of the alloys.

Typical etched microstructures of Ti-Zr-Mo-Cu alloys are revealed by SEM images shown in Fig. 2. Ti-Zr-Mo-Cu alloys exhibit equiaxed β grains, and the grain size decreases with increasing Mo content, which is consistent with the finding that Mo promotes refinement of the prior β phase [23]. Mo as a solution prevents the grain boundary movement that affects both the nucleation and growth of recrystallizing grains [24]. The observed contrast variations between grain boundaries and the grain interiors indicate potential elemental segregation occurring during solidification [25]. Fig. 3 shows SEM-EDS analysis results from 8Mo alloy, indicating that grain interiors are a Ti-Mo-rich (β) phase, while Zr and Cu elements have obvious segregation in grain boundaries.

The representative TEM micrographs, selective electron diffraction patterns (SAED) and EDS maps of 6Mo, 8Mo and 17Mo alloys are shown in Fig. 4. Fig. 4(a-b) shows HAADF TEM image and corresponding SAED pattern of 6Mo alloy, which consists of a β-phase with BCC structure, lath-shaped α'' phase with orthorhombic structure and ω phase (trigonal [26]). In titanium-based alloys, the metastable ω-phase often coexists with the α''-phase [27]. According to its formation pathways, the ω-phase could be classified into two distinct modes: thermal ω (resulting from rapid cooling-induced diffusionless transformation) and isothermal ω phase (developed during subsequent aging treatments). In the 6Mo alloy, the relatively low content of the strong β-stabilizing element Mo compromises the stability of the β-phase. During cooling, fine-scale athermal ω phases precipitate within the matrix via a

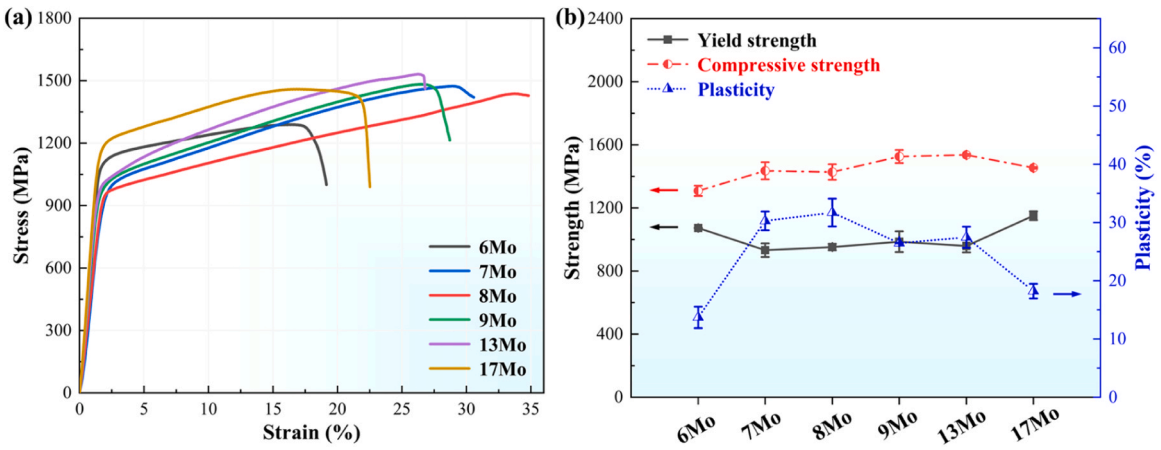

Fig. 5. Mechanical properties of the Ti-18Zr-xMo-10Cu alloys. (a) Engineering stress-strain curves at room temperature. (b) Summarized yield strength, compressive strength, and plasticity values.

diffusionless transformation mechanism. Due to the nanoscale dimensions and highly dispersed distribution of both ω and α″ phases, conventional X-ray diffraction (XRD) techniques lack sufficient sensitivity for their detection. In Fig. 4(d), a bright-field (BF) image of 8Mo alloy reveals a lath-shaped α″ phase (10–20 nm in width and 100–150 nm in length) dispersed within *β*-phase. The SAED pattern further corroborates the absence of athermal ω phases within the matrix. This finding is consistent with the previously reported phase evolution trend in ternary Ti-Zr-Mo alloys [23], wherein Mo acts as an effective inhibitor of ω-phase stabilization. A monotonic weakening of ω-phase diffraction intensities is observed with elevated Mo concentrations, culminating in their elimination beyond a critical threshold. EDS analysis demonstrates that Cu and Zr are enriched in the α″ phases, while the *β*-phase is predominantly rich in Ti and Mo (Fig. 4(c, f)). The 17Mo alloy exhibits continuous precipitation of acicular α″-phase at grain boundaries, as confirmed by SAED analysis (Fig. 4(g)). Intragranular regions reveal lamellar Zr_2Cu precipitates, identified through SAED pattern indexing (Fig. 4(h)). No evidence of the ω phase is detected, indicating its suppression under this composition. Compared to other alloys in the system, secondary phases in the 17Mo variant predominantly accumulate at grain boundaries with a pronounced intergranular segregation. The pronounced deterioration in ductility stems from the inherent brittleness of Zr_2Cu/α″-phase interfaces, where localized stress concentrations activate dual degradation pathways: intergranular embrittlement *via* interfacial decohesion and transgranular crack propagation nucleated at phase boundary triple junctions.

3.2. Mechanical properties and fractography

As research demonstrates, alloy microstructure directly influences strength, toughness, elastic modulus, and plasticity [28–30]. Mechanical properties of the Ti-18Zr-xMo-10Cu alloys were obtained using uniaxial compressive tests and microhardness measurements. Fig. 5(a) shows the engineering stress-strain curves of the 6Mo, 7Mo, 8Mo, 9Mo, 13Mo, and 17Mo alloys. From the stress-strain curves, the yield strength, compressive strength, and plasticity are summarized in Fig. 5(b). The 6Mo alloy achieves a yield strength of 1073 MPa and a compressive strength of 1308 MPa, but its fracture strain remains limited to 13.7 %, indicating restricted plasticity. The tradeoff between strength and plasticity requires precisely tailored microstructure, such as *β*-phase refinement and interfacial segregation through guided alloy design, to achieve a balanced enhancement of mechanical properties. Both the compressive strength and plasticity values increase up to 7Mo alloy, then, they increase with the Mo content and a peak is almost observed at 8Mo alloy, despite a slight decrease in yield strength. Higher Mo content stabilizes the *β*-phase while suppressing the precipitation of ω-phase and

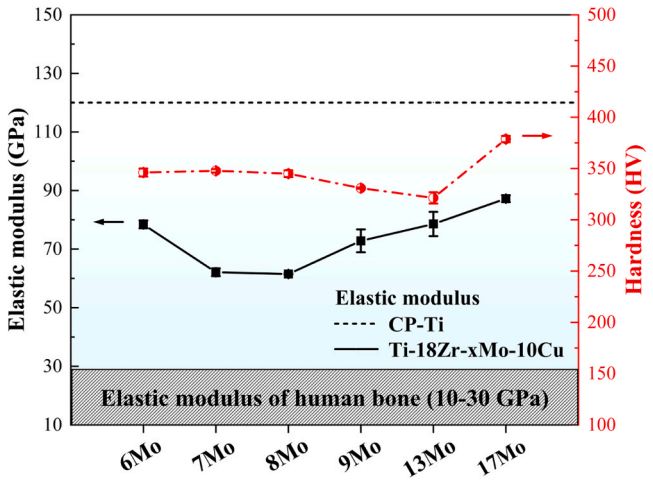

Fig. 6. Elastic modulus and vicker's hardness of Ti-18Zr-xMo-10Cu alloys.

α″-phase, thereby improving plasticity [23]. When the Mo content further increases to 17 wt%, the yield strength and compressive strength reach 1151 MPa and 1454 MPa, respectively, but the fracture strain drops to 18.2 %. The morphological transition of α″-phase, from homogeneously dispersed lath-shaped precipitates to *β* grain boundary-aligned lamellae, creates interfacial mechanical property disparities due to compositional disparity with the *β* matrix. These disparities generate localized back stresses that hinder dislocation motion, enhancing yield strength. During plastic deformation, grain boundary-α″ lamellae in the 17Mo alloy promotes rapid dislocation pile-up at interfaces, initiating localized stress concentration. This micromechanical response facilitates premature crack nucleation and propagation through weakened grain boundaries, severely degrading ductility and inducing intergranular brittle fracture.

Fig. 6 presents the variation of elastic modulus and hardness in the developed alloys. It should be noted that the design strategy aims to achieve a bone-like elastic modulus (~30 GPa [20,27,31]) while retaining high strength, plasticity, and hardness, thereby removing stress shielding, which may result in implant loosening and periprosthetic fracture [1]. As reported, the α″ phase transformation leads to a decrease in the yield [32], while ω-precipitation may lead to dramatically decreased plasticity and increased elastic modulus [33]. Metastable *β*-phase exhibited the lowest modulus among all phases [34]. Notably, the 8Mo alloy, the most retained β-phase due to suppressed phase transformation exhibits the lowest elastic modulus (~60 GPa). In

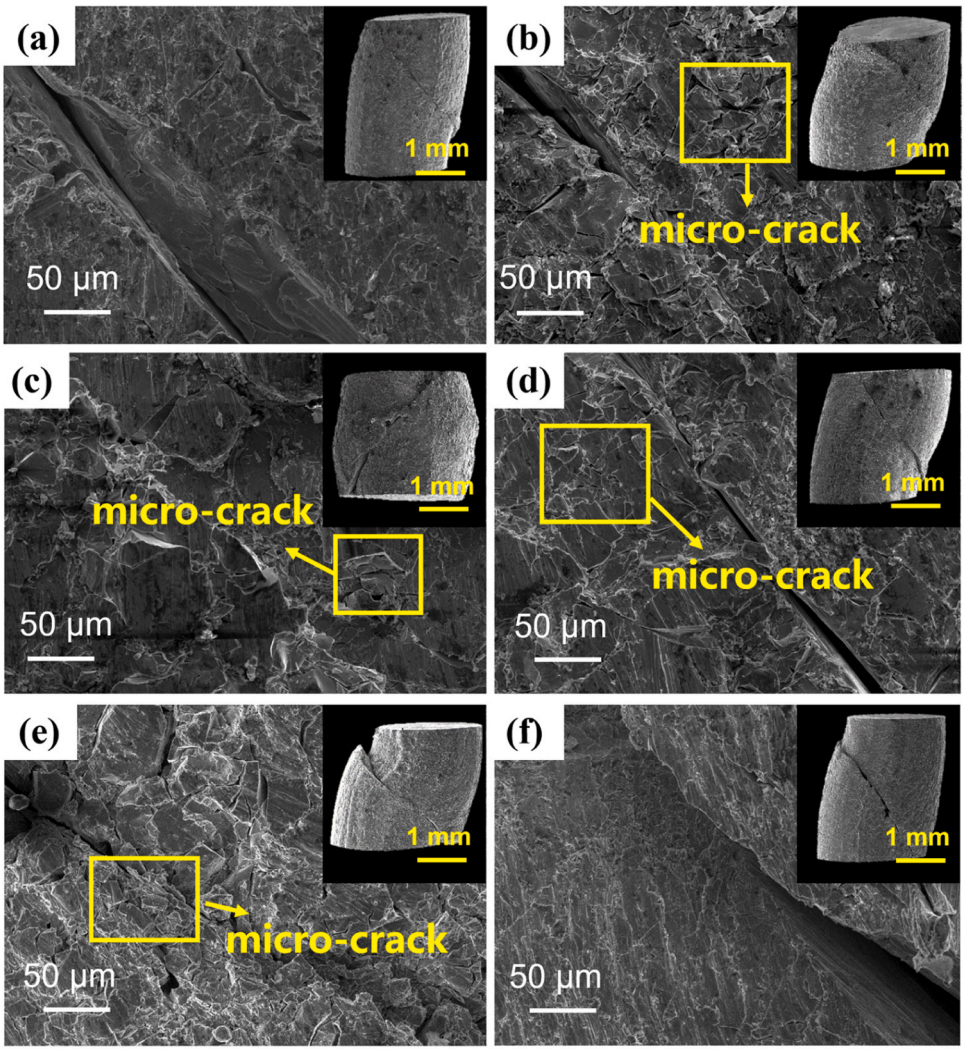

Fig. 7. SEM fractographs of (a) 6Mo alloy, (b) 7Mo alloy, (c) 8Mo alloy, (d) 9Mo alloy, (e) 13Mo alloy, and (f) 17Mo alloy showing the height of the compressed specimen and stress concentration induced microcrack.

contrast, the 17Mo alloy demonstrates the highest elastic modulus due to dense α''-phase precipitations and Zr_2Cu intermetallic formation at both intragranular and grain boundary regions. Quantitative analysis the volume fractions of β-phases and precipitates were performed on over ten TEM micrographs per alloy condition using Image J software. The approximate volume fractions of β-phase in 6Mo, 8Mo, and 17Mo alloys is 83.53 %, 89.41 %, and 74.39 %, respectively. The corresponding precipitates approach ~17 %, ~10 %, and ~26 %, respectively. A decrease in elastic modulus was observed with decreasing precipitates, establishing a direct correlation between microstructural evolution and mechanical properties. The 6Mo alloy exhibits a secondary peak in elastic modulus, which is attributed to a small number of ω-phase precipitation. Additionally, the 8Mo alloy retains better hardness values (~350 HV), which substantially exceed those of conventional titanium alloy (~182 HV [35]). It is known that alloys with higher hardness exhibit superior wear resistance, as hardness plays a critical role in resisting plastic deformation and abrasive wear mechanisms. Generally, the integration of low elastic modulus, high strength, large plasticity, and high hardness of the novel 8Mo HEAs are favorable for biomedical applications.

SEM images of the post-compression specimens and the microstructural features adjacent to the primary crack are shown in Fig. 7. In 6Mo and 17Mo alloys, the fracture along a 45° inclination angle exhibits only a single dominant crack on the surface with poor plastic deformation, indicating a brittle fracture mechanism. While the 7Mo~13Mo alloys show upsetting behavior and secondary cracks are observed on the fracture surface alongside the primary crack. The deformation amount initially increases and subsequently decreases with rising Mo content, a trend consistent with the variation in fracture strain. Further, the fracture surface of 6Mo, 8Mo, and 17Mo alloys are shown in Fig. 8. The presence of plasticity-induced cleavage steps has been observed in 6Mo alloy (Fig. 8(a-b)). Ductile fractures frequently show voids, inclusions, or forms of apparently extended dimples, as displayed in 8Mo alloy (Fig. 8(c-d)), indicating that 8Mo alloy has relatively high plasticity, which can be attributed to the decreased α'' and ω precipitations. As given in Fig. 8(e-f) (17Mo alloy), numerous tear ridges are found. Long microcracks could originate from grain boundary and then expand, indicating that the existence of numerous hard phases, such as α'' and Zr_2Cu intermetallic, obviously decreased the plasticity of 17Mo alloy.

3.3. Corrosion behavior

To characterize the corrosion behavior of the Ti-Zr-Mo-Cu alloys, electrochemical measurements on these alloys and the pure Ti are conducted in Hank's solution for simulating the body fluid environment. The changes in the open-circuit potentials (OCPs) with elapsed time of the alloys are exhibited in Fig. 9(a). The OCPs of these alloys undergo an

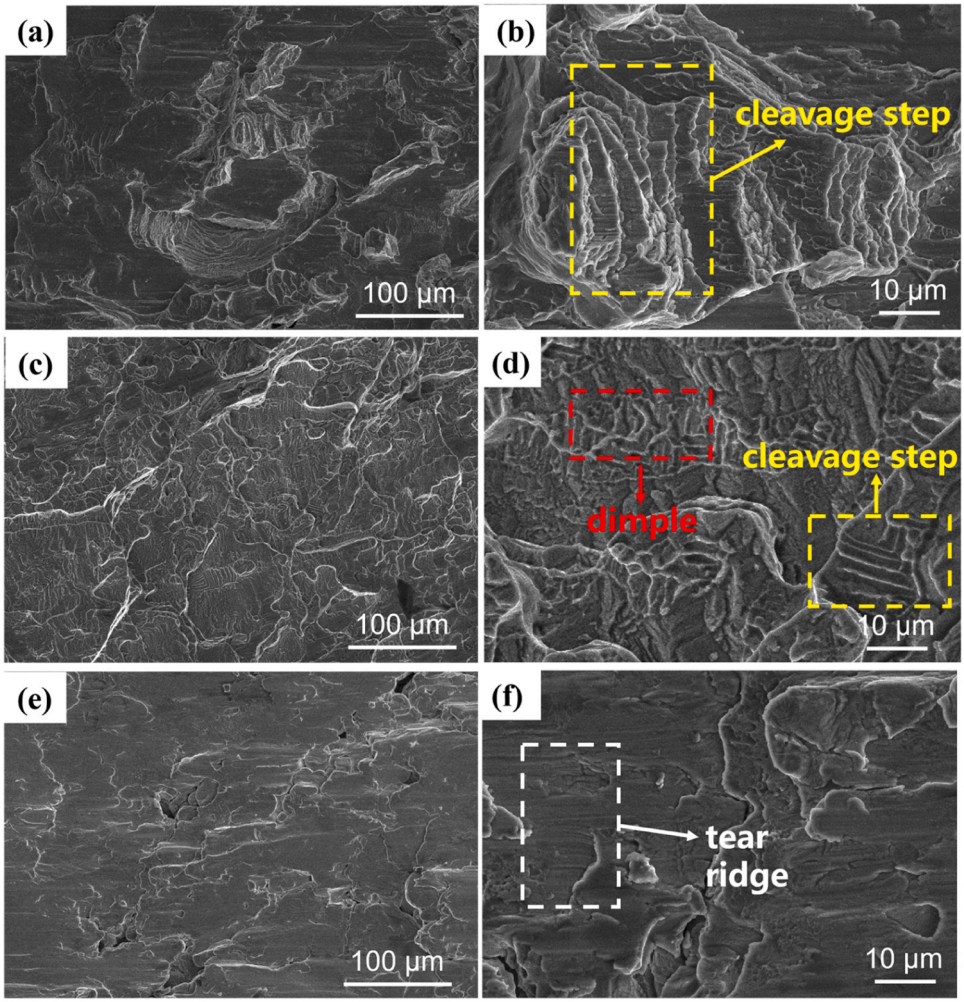

Fig. 8. SEM fractographs of (a-b) 6Mo alloy, (c-d) 8Mo alloy, (e-f) 17Mo alloy showing plasticity-induced cleavage steps, dimple, and tear ridge with increasing Mo content.

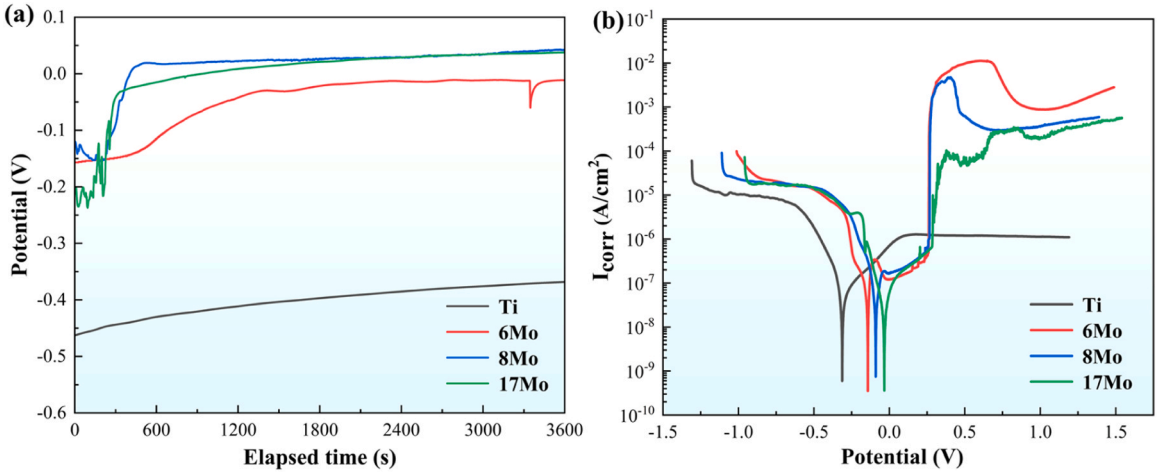

Fig. 9. (a) Changes in the open circuit potential (OCP) with immersion time and (b) potentiodynamic-polarization curves of pure Ti, 6Mo, 8Mo, and 17Mo alloys in Hank's solution.

initial positive potential offset followed by steady values, demonstrating enhanced passivation kinetics and progressive densification of surface oxide films during prolonged immersion. After 3600 s, the 6Mo, 8Mo, and 17Mo possess higher OCP of about −0.1–0.05 V than pure Ti alloy (~-0.4 V). It implies that the stability of the surface films on our alloys exhibits an improving tendency. Fig. 9(b) shows the potentiodynamic-polarization plots of the Ti-Zr-Mo-Cu alloys and the Ti alloy. Our alloys are spontaneously passivated with passive current densities around

Table 1
Electrochemical parameters of Ti-18Zr-xMo-10Cu (x = 6, 8, 17 wt%) alloys and Ti alloy.

Samples	E_{corr} (mV)	I_{corr} (nA/cm^{-2})	I_{pass} (μA/cm^{-2})
6Mo	−143	27.1	0.288
8Mo	−93	23.8	0.386
17Mo	−36	12.7	0.369
Ti	−311	21.2	1.310

10^{-4}~10^{-2} A/cm^2, then the secondary passivation occurs as revealed by the abrupt rise in the current density at the potential of ~0.25 V, and no pitting corrosion was observed. The corrosion parameters derived from the polarization curves are summarized in Table 1. As the Mo content in the alloy decreases, the corrosion potentials show a decreasing trend yet nobler than pure Ti, while the corrosion current densities remain at 10^{-3} A/cm^2 and show no distinguishable difference. These results indicate the good bio-corrosion resistance of 8Mo alloy in the aggressive physiological fluid. It is reported that Mo enhances the passivation capability of alloys through the formation of a protective layer composed of MoO_2 and MoO_4^{2-} ions [36]. In addition, the microstructure could be a critical factor of corrosion resistance that Ti-18Zr-13Mo alloy with a homogeneous single β-phase microstructure and refined grain structure exhibited superior corrosion resistance than binary Ti-13Mo and Ti-18Zr alloys in simulated physiological environments [35]. Chen et al. further demonstrate that selective laser melted (SLM) Ti-6Al-4V alloys with suppressed α-phase content and predominant β-phase distribution exhibit enhanced corrosion resistance in 3.5 wt% NaCl solution, as evidenced by a 50 % reduction in corrosion current density compared to conventionally cast counterparts [37].

The EIS impedance measurement provided detailed data characterization of the electrochemical performance and the corresponding characterization curves are obtained in Fig.10. In the Nyquist curves (Fig. 10(a)), all Ti-Zr-Mo-Cu alloys exhibit a single-capacitance feature. Compared to the pure Ti and 6Mo alloys, 8Mo and 17Mo alloys have a larger arc radius size, which is mostly due to the higher interfacial charge transfer resistance, and signifies the lower electrical conductivity. A higher interfacial charge transfer resistance results in greater difficulty in the charge transfer process, corresponding to an increased capacitive arc radius, which indicates superior corrosion resistance of the alloy [38,39]. In other words, the higher Mo content increases the corrosion resistance. By observing the Bode phase angle diagrams (Fig. 10(b)), it can be seen that the moduli of impedance are independent at high-frequency range from 10^5 down to 10^3 Hz, and phase angle approach to 0° (Fig. 10(c)). This frequency range demonstrated a resistive behavior corresponding to the solution resistance between the working and the reference electrode [40]. At medium and low-frequency (10^{-1}~10^2 Hz), a flat portion of the curves is observed in the Bode plot (Fig. 10(c)), which is due to the response of the high stability of the passive film. Li et al. [40] explained that the high capacitive behavior could be observed by the maximum phase angle approaching 90° in the low-frequency region, which reveals the highly compact oxide film. Therefore, the low-frequency phase shift moves from ~80° in Ti-Zr-Mo-Cu alloys to a lower degree of 75° in Ti alloy, indicating the increased corrosion resistance of our alloys. To give quantitative support to the EIS data, the impedance parameters of the double layer are modeled with a well-known electrical equivalent circuit (EEC) for Ti and Ti-Zr-Mo-Cu alloys [41–43]. In this model (Fig. 10(c)),

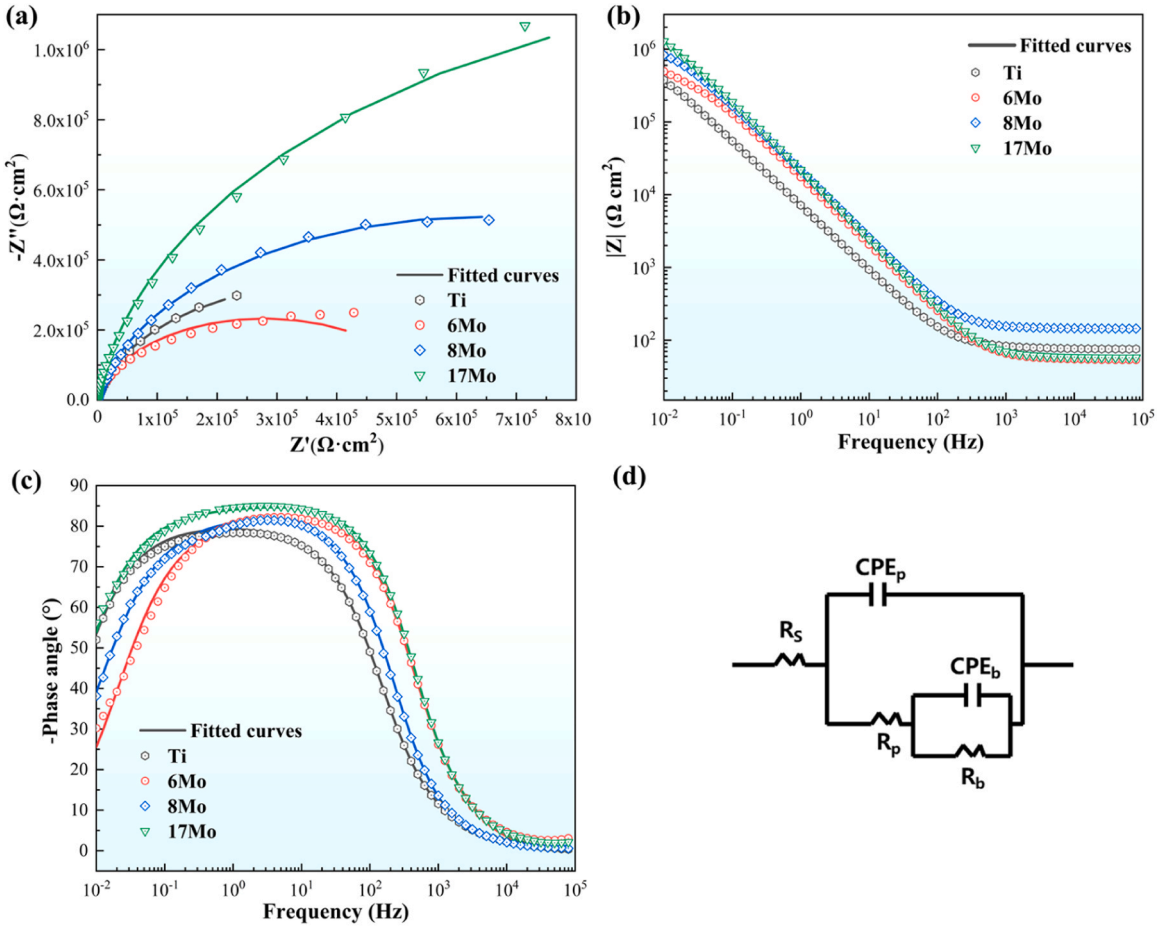

Fig. 10. Ti-18Zr-xMo-10Cu (x = 6, 8, 17 wt%) alloy in SBF solution. (a) Nyquist plots, (b) Bode impedance magnitude plots, (c) Bode phase angle plots, and (d) Equivalent circuit model.

Table 2
The fitted impedance parameters of Ti-18Zr-xMo-10Cu (x = 6, 8, 17 wt%) alloys and Ti as the control in Hank's solution.

Samples	R_s ($\Omega\cdot cm^2$)	CPE_p ($\mu F\cdot cm^{-2}$)	R_p ($\Omega\cdot cm^2$)	CPE_b ($\mu F\cdot cm^{-2}$)	R_b ($K\Omega\cdot cm^2$)
6Mo	54.41	3.16	58.38	7.99	563.6
8Mo	96.92	1.01	50.05	7.93	1363.4
17Mo	57.97	2.87	49.25	5.39	2642.3
Ti	114.0	9.13	58.50	3.68	3442.3

R_s represents the resistances of solution between the reference electrode and the working electrode, R_p and R_b are the resistances of outer and inner layers [44], respectively, which comprise the charge transfer resistance through the outer layer and with the participation of adsorbed intermediates. The CPE_p and CPE_b correspond to the capacitance of the outer layer and the capacitance of the inner layer associated with the double-layer formation [44]. A constant-phase element (CPE) is used rather than an ideal capacitor, to account for the non-ideal behavior of the capacitive element. Table 2 gives the values of circuit parameters for the 6Mo, 8Mo, 17Mo, and Ti alloys, obtained *via* fitting the EEC on the experimental EIS data. The inner layer resistance (R_b) ranged from 5.636×10^5 to 3.442×10^6 $\Omega\cdot cm^2$ demonstrating significantly higher values than the outer porous layer resistance (R_p = 49.25–58.50 $\Omega\cdot cm^2$), confirming that the corrosion resistance of both the alloys and Ti predominantly originates from the protective characteristics of the dense inner oxide layer. Furthermore, the value of R_b increases with increasing Mo content of Ti-18Zr-xMo-10Cu (x = 6, 8, 17 wt%) alloys, demonstrating that Mo addition effectively enhances the corrosion resistance. Accordingly, the impedance spectra, fitted impedance parameters, and polarization curve results exhibit consistent trends, confirming improved corrosion resistance with increasing Mo content.

4. Conclusion

In this study, a composition design approach was applied to explore novel Ti-Zr-Mo-Cu multi-principal element alloys that achieve multiple desirable attributes, i.e., high strength, large plasticity, ultra-low elastic modulus, and good corrosion resistance. This design tunes the stability of the β-phase under subtle conditions via higher β-stabilizing element Mo content that helps to limit the α''/ω precipitations within the matrix and restrict the size of the precipitations. However, the β-stabilizing effect of Mo exhibits a non-monotonic tendency, and the excessive Mo addition may induce the formation of detrimental secondary phases, such as Zr_2Cu intermetallic compounds in 17Mo alloy. Optimal 8Mo alloy exhibited a true peak compressive strength of ~1400 MPa, the plastic strain of ~35 % along with the lower elastic modulus. The corrosion potential and current density of the Ti-Zr-Mo-Cu alloys increase with higher Mo content, which leads to an increase in corrosion resistance. The corrosion resistance is ranked 17Mo> 8Mo> 6Mo alloy. In general, the 8Mo alloy exhibits substantial potential as the advancement of biomedical alloys that combine a lower elastic modulus with high strength, large plasticity, and sufficient corrosion resistance.

CRediT authorship contribution statement

Qianqian Wang: Investigation. **Qihan Zheng:** Investigation, Data curation. **Baolong Shen:** Supervision, Project administration, Funding acquisition. **Zhijun Guo:** Writing – review & editing, Methodology, Funding acquisition. **Minqi Xu:** Methodology, Investigation, Data curation. **Yusha Luo:** Writing – original draft, Visualization, Investigation, Formal analysis, Data curation.

Declaration of Competing Interest

The authors declare that they have no known competing financial interests or personal relationships that could have appeared to influence the work reported in this paper.

Acknowledgments

This work was supported by the National Natural Science Foundation of China (52231005, 52001324) and the Start-up Research Fund of Southeast University (RF1028623113), Open Research Fund of Jiangsu Key Laboratory of Advanced Metallic Materials, Southeast University (No. AMM2025A01, AMM2024A02, AMM2023B05).

Research data

Due to the sensitive nature of the questions asked in this study, survey respondents were assured raw data would remain confidential and would not be shared.

Data Availability

Due to the sensitive nature of the questions asked in this study, survey respondents were assured raw data would remain confidential and would not be shared.

References

[1] S.S. Sidhu, H. Singh, M.A.-H. Gepreel, A review on alloy design, biological response, and strengthening of β-titanium alloys as biomaterials, Mater. Sci. Eng. C 121 (2021) 111661.
[2] S. Hussenbocus, D. Kosuge, L.B. Solomon, D.W. Howie, R.H. Oskouei, Head-neck taper corrosion in hip arthroplasty, Biomed. Res. Int. 2015 (2015) 758123.
[3] M. Geetha, A.K. Singh, R. Asokamani, A.K. Gogia, Ti based biomaterials, the ultimate choice for orthopaedic implants, Prog. Mater. Sci. 54 (2009) 397–425.
[4] L.C. Zhang, L.Y. Chen, A review on biomedical titanium alloys: recent progress and prospect, Adv. Eng. Mater. 21 (2019) 1801215.
[5] X. Tong, Q. Sun, D. Zhang, K. Wang, Y. Dai, Z. Shi, Y. Li, M. Dargusch, S. Huang, J. Ma, C. Wen, J. Lin, Impact of scandium on mechanical properties, corrosion behavior, friction and wear performance, and cytotoxicity of a beta-type Ti-24Nb-38Zr-2Mo alloy for orthopedic applications, Acta Biomater. 134 (2021) 791–803.
[6] A. Chmielewska, D. Dean, The role of stiffness-matching in avoiding stress shielding-induced bone loss and stress concentration-induced skeletal reconstruction device failure, Acta Biomater. 173 (2024) 51–65.
[7] B. Liu, Z. Ma, J. Li, H. Xie, X. Wei, B. Wang, S. Tian, J. Yang, L. Yang, L. Cheng, L. Li, D. Zhao, Experimental study of a 3D printed permanent implantable porous Ta-coated bone plate for fracture fixation, Bioact. Mater. 10 (2022) 269–280.
[8] C.E. Wen, Y. Yamada, K. Shimojima, Y. Chino, H. Hosokawa, M. Mabuchi, Novel titanium foam for bone tissue engineering, J. Mater. Res. 17 (2002) 2633–2639.
[9] X. Yang, C.R. Hutchinson, Corrosion-wear of beta-Ti alloy TMZF (Ti-12Mo-6Zr-2Fe) in simulated body fluid, Acta Biomater. 42 (2016) 429–439.
[10] J. Davidson, A. Mishra, P. Kovacs, R. Poggie, New surface-hardened, low-modulus, corrosion-resistant Ti-13Nb-13Zr alloy for total hip arthroplasty, Biomed. Mater. Eng. 4 (1994) 231–243.
[11] W. Yang, S. Pang, Y. Liu, Q. Wang, P.K. Liaw, T. Zhang, Design and properties of novel Ti-Zr-Hf-Nb-Ta high-entropy alloys for biomedical applications, Intermetallics 141 (2022) 107421.
[12] Y. Wu, Y. Zhang, Z. Li, Z. Liu, E. Zhao, J. Liu, Prediction of NbTaTiZr-based high-entropy alloys with high strength or ductility: first-principles calculations, J. Mater. Res. Technol. 30 (2024) 8854–8861.
[13] Z. Ke, C. Yi, L. Zhang, Z. He, J. Tan, Y. Jiang, Characterization of a new Ti-13Nb-13Zr-10Cu alloy with enhanced antibacterial activity for biomedical applications, Mater. Lett. 253 (2019) 335–338.
[14] X.-Y. Zhao, R.-R. Chen, Y. Yang, J.-J. Guo, H.-S. Ding, Y.-Q. Su, H.-Z. Fu, Microstructure and mechanical properties of Ti43Al6Nb alloys with different zirconium contents, Rare Met. 42 (6) (2018) 2047–2056.
[15] J. Yang, M. Baatarsukh, J. Bae, S. Huh, H. Jeong, B. Choi, T. Nam, J. Noh, Phase stability and properties of Ti-Nb-Zr thin films and their dependence on Zr addition, Materials 11 (2018) 1361.
[16] Kun Yang Xiang Xiao, Dechuang Zhang Shan Lei, Yilong Dai Lin Guo, J. Lin, A β-type titanium alloy with high strength and low elastic modulus achieved by spinodal decomposition, J. Alloy. Compd. 963 (2023) 171270.
[17] P. Laheurte, F. Prima, A. Eberhardt, T. Gloriant, M. Wary, E. Patoor, Mechanical properties of low modulus beta titanium alloys designed from the electronic approach, J. Mech. Behav. Biomed. Mater. 3 (2010) 565–573.
[18] T.K. Jung, S. Semboshi, N. Masahashi, S. Hanada, Mechanical properties and microstructures of beta Ti-25Nb-11Sn ternary alloy for biomedical applications, Mater. Sci. Eng. C Mater. Biol. Appl. 33 (2013) 1629–1635.
[19] S. Bahl, S. Suwas, K. Chatterjee, Comprehensive review on alloy design, processing, and performance of β Titanium alloys as biomedical materials, Int. Mater. Rev. 66 (2020) 114–139.

[20] Q. Chen, G.A. Thouas, Metallic implant biomaterials, Mater. Sci. Eng. R. 87 (2015) 1–57.
[21] Y.L. Hao, S.J. Li, S.Y. Sun, R. Yang, Effect of Zr and Sn on Young's modulus and superelasticity of Ti-Nb-based alloys, Mater. Sci. Eng. A 441 (2006) 112–118.
[22] P.J. Bania, Beta titanium alloys and their role in the titanium industry, JOM 46 (1994) 16–19.
[23] X. Zhao, M. Niinomi, M. Nakai, T. Ishimoto, T. Nakano, Development of high Zr-containing Ti-based alloys with low Young's modulus for use in removable implants, Mater. Sci. Eng. C. 31 (2011) 1436–1444.
[24] F.J. Humphreys, M. Hatherly, Recrystallization and Related Annealing Phenomena, Elsevier, Kidlington, 2004.
[25] N. Yumak, K. Aslantaş, A review on heat treatment efficiency in metastable β titanium alloys: the role of treatment process and parameters, J. Mater. Res. Technol. 9 (2020) 15360–15380.
[26] B. Qian, X. Li, Y. Wang, J. Hou, J. Liu, S. Zou, F. An, W. Lu, An ultra-low modulus of ductile TiZrHfTa biomedical high-entropy alloys through deformation induced martensitic transformation/twinning/amorphization, Adv. Mater. 36 (24) (2024).
[27] Y. Tian, L. Zhang, D. Wu, R. Xue, Z. Deng, T. Zhang, L. Liu, Achieving stable ultra-low elastic modulus in near-β titanium alloys through cold rolling and pre-strain, Acta Mater. 286 (2025).
[28] D. Li, S.-X. Hui, W.-J. Ye, C.-L. Li, Microstructure and mechanical properties of a new high-strength and high-toughness titanium alloy, Rare Met. 42 (1) (2016) 281–287.
[29] Zhongde Zhang, Yanghe Wang, Zhipeng Pi, Jianguo Lin, D. Zhang, Phase field simulation of martensitic transformation in Ti-24Nb-4Zr-8Sn alloy, Smart Mat. 1 (2023) 100017.
[30] Guo He, Jürgen Eckert, Wolfgang Löser, L. Schultz, Novel Ti-base nanostructure-dendrite composite with enhanced plasticity, Nat. Mater. 2 (2003) 33–37.
[31] Z. Hua, D. Zhang, L. Guo, S. Lin, Y. Li, C. Wen, Medium-entropy Zr-Nb-Ti alloys with low magnetic susceptibility, high yield strength, and low elastic modulus through spinodal decomposition for bone-implant applications, Acta Biomater. 190 (2024) 623–641.
[32] K. Chen, Q. Fan, J. Yao, L. Yang, S. Xu, W. Lei, D. Wang, J. Yuan, H. Gong, X. Cheng, Composition design of a novel Ti-6Mo-3.5Cr-1Zr alloy with high-strength and ultrahigh-ductility, J. Mater. Sci. Technol. 131 (2022) 276–286.
[33] R. Kondo, N. Nomura, Suyalatu, Y. Tsutsumi, H. Doi, T. Hanawa, Microstructure and mechanical properties of as-cast Zr-Nb alloys, Acta Biomater. 7 (2011) 4278–4284.
[34] Y.L. Zhou, M. Niinomi, T. Akahori, Decomposition of martensite α'' during aging treatments and resulting mechanical properties of Ti-Ta alloys, Mater. Sci. Eng. A 384 (2004) 92–101.
[35] Z. Guo, Y. Huang, C. Sun, Z. He, Y. Li, H. Qiu, D. Yuan, J. Zhang, C. Chu, B. Shen, Preparation and characterization of metastable β-type titanium alloys with favorable properties for orthopedic applications, J. Alloy. Compd. 949 (2023) 169839.
[36] M.A. Ameer, A.M. Fekry, F.E.-T. Heakal, Electrochemical behaviour of passive films on molybdenum-containing austenitic stainless steels in aqueous solutions, Electrochim. Acta 50 (2004) 43–49.
[37] G. Chen, Q. Zhai, Z. Ma, X. Yin, Q. Zhang, H. Zhou, L. Meng, K. Wang, S. Wang, L. Wang, Effect of Cr content on microstructure, mechanical properties and corrosion behavior of Ti6Al4V alloy produced by selective laser melting, Mater. Technol. 37 (2021) 1062–1074.
[38] M.A. Siddiqui, I. Ullah, S.K. Kolawole, C. Peng, J. Wang, L. Ren, K. Yang, D. D. Macdonald, Study the existing form of copper (p-type oxide/segregation) and its release mechanism from the passive film of Ti-7Cu alloy, Corros. Sci. 190 (2021).
[39] M.A. Siddiqui, I. Ullah, H. Liu, S. Zhang, L. Ren, K. Yang, Preliminary study of adsorption behavior of bovine serum albumin (BSA) protein and its effect on antibacterial and corrosion property of Ti-3Cu alloy, J. Mater. Sci. Technol. 80 (2021) 117–127.
[40] J. Li, S.J. Li, Y.L. Hao, R. Yang, Electrochemical characterization of nanostructured Ti-24Nb-4Zr-8Sn alloy in 3.5% NaCl solution, Int. J. Hydrog. Energy 39 (2014) 17452–17459.
[41] J.E.G. Gonzalez, J.C. Mirza-Rosca, Study of the corrosion behavior of titanium and some of its alloys for biomedical and dental implant applications, J. Electroanal. Chem. 471 (1999) 109–115.
[42] A. Macpherson, X. Li, P. McCormick, L. Ren, K. Yang, T.B. Sercombe, Antibacterial titanium produced using selective laser melting, JOM 69 (2017) 2719–2724.
[43] Y. Li, J. Xu, Is niobium more corrosion-resistant than commercially pure titanium in fluoride-containing artificial saliva? Electrochim. Acta 233 (2017) 151–166.
[44] W.R. Osório, A. Cremasco, P.N. Andrade, A. Garcia, R. Caram, Electrochemical behavior of centrifuged cast and heat treated Ti-Cu alloys for medical applications, Electrochim. Acta 55 (2010) 759–770.